

Evaluation of a large-eddy model simulation of a mixed-phase altocumulus cloud using microwave radiometer, lidar and Doppler radar data

By J. H. MARSHAM¹*, S. DOBBIE¹ and R. J. HOGAN²

¹*Institute for Atmospheric Science, University of Leeds, UK*

²*Department of Meteorology, University of Reading, UK*

(Received 8 July 2005; revised 22 February 2006)

SUMMARY

Using the Met Office large-eddy model (LEM) we simulate a mixed-phase altocumulus cloud that was observed from Chilbolton in southern England by a 94 GHz Doppler radar, a 905 nm lidar, a dual-wavelength microwave radiometer and also by four radiosondes. It is important to test and evaluate such simulations with observations, since there are significant differences between results from different cloud-resolving models for ice clouds. Simulating the Doppler radar and lidar data within the LEM allows us to compare observed and modelled quantities directly, and allows us to explore the relationships between observed and unobserved variables. For general-circulation models, which currently tend to give poor representations of mixed-phase clouds, the case shows the importance of using: (i) separate prognostic ice and liquid water, (ii) a vertical resolution that captures the thin layers of liquid water, and (iii) an accurate representation the subgrid vertical velocities that allow liquid water to form.

It is shown that large-scale ascents and descents are significant for this case, and so the horizontally averaged LEM profiles are relaxed towards observed profiles to account for these. The LEM simulation then gives a reasonable cloud, with an ice-water path approximately two thirds of that observed, with liquid water at the cloud top, as observed. However, the liquid-water cells that form in the updraughts at cloud top in the LEM have liquid-water paths (LWPs) up to half those observed, and there are too few cells, giving a mean LWP five to ten times smaller than observed. In reality, ice nucleation and fallout may deplete ice-nuclei concentrations at the cloud top, allowing more liquid water to form there, but this process is not represented in the model. Decreasing the heterogeneous nucleation rate in the LEM increased the LWP, which supports this hypothesis.

The LEM captures the increase in the standard deviation in Doppler velocities (and so vertical winds) with height, but values are 1.5 to 4 times smaller than observed (although values are larger in an unforced model run, this only increases the modelled LWP by a factor of approximately two). The LEM data show that, for values larger than approximately 12 cm s^{-1} , the standard deviation in Doppler velocities provides an almost unbiased estimate of the standard deviation in vertical winds, but provides an overestimate for smaller values. Time-smoothing the observed Doppler velocities and modelled mass-squared-weighted fallspeeds shows that observed fallspeeds are approximately two-thirds of the modelled values. Decreasing the modelled fallspeeds to those observed increases the modelled IWC, giving an IWP 1.6 times that observed.

KEYWORDS: Cloud radar Cloud-resolving model Ice nuclei

1. INTRODUCTION

Altocumulus and altostratus clouds cover approximately 22% of the earth's surface (Warren *et al.* 1986, 1988) and play an important role in the climate system (Li and Le Treut 1992; Sun and Shine 1995). Mixed-phase layer clouds are, however, often poorly represented in numerical weather prediction models (Hogan *et al.* 2003b; Vailancourt *et al.* 2003; Tremblay and Glazer 2000; Tremblay *et al.* 2003). Cloud-resolving model (CRM) simulations of such clouds should allow us to understand the processes that must be included to model these clouds in general-circulation models (GCMs) and so lead to improved GCM parametrizations. Despite this, there are remarkably few published CRM simulations of mixed-phase altocumulus or altostratus clouds using high spatial resolutions (i.e. horizontal grid spacings of less than 1 km). Clark *et al.* (2005) explored the sensitivity of a large-eddy model (LEM) to changes in microphysics for

* Corresponding author: Institute for Atmospheric Science, School of the Earth and Environment, University of Leeds, Leeds LS2 9JT, UK. e-mail: jmarsham@env.leeds.ac.uk

a frontal mixed-phase cloud; Starr and Cox (1985) and Liu and Krueger (1995, 1998) simulated similar liquid-phase altostratus or altocumulus clouds; and Cotton and Brown (2004) applied their prognostic ice-nuclei scheme to an idealized mixed-phase altostratus cloud. Of these simulations, only Clark *et al.* (2005) directly compared results with observations. Starr *et al.* (2000) showed a considerable variation between CRMs for cirrus clouds, and we might expect a similar variation for stratiform mixed-phase clouds. As a result, it is currently important to evaluate CRMs by comparing their results with observations.

In this paper we simulate a case of mixed-phase altocumulus observed by the 94 GHz radar and 905 nm lidar at Chilbolton in southern England using the Met Office LEM. To evaluate the ability of the LEM to represent a mixed-phase cloud we compare fields of observed and modelled variables. For the lidar and Doppler radar data this requires us to simulate the data within the LEM to account for the temporal and spatial sampling of the instruments. This then allows relationships between observed parameters (such as Doppler velocities) and unobserved parameters (such as fallspeeds and air velocities) to be explored, giving a better understanding of the observed quantities.

There have been several recent observational studies of mixed-phase layer clouds (Heymsfield *et al.* 1991; Fleishauer *et al.* 2002; Korolev and Isaac 2003; Hogan *et al.* 2003a,b, 2004; Field *et al.* 2004) that have utilized both ground-based lidar and radar, as well as aircraft data. *In situ* measurements are invaluable for validating CRMs, but cloud observing radars and lidars are a very important source of data, since they are capable of continuously retrieving profiles of cloud parameters. Thus, they produce two-dimensional (space–time) fields, with similar spatial and temporal resolution to CRMs. In particular, whilst the radar can be used to retrieve ice-water content (IWC) and fallspeeds, the lidar data indicate the position of any liquid-water layers (which tend to be very reflective because of the small size and high number concentration of the supercooled water droplets compared with the ice particles). One limitation of such radars and lidars are their fixed location, but the CloudSat* and Calipso† instruments will soon give an unprecedented volume and spatial coverage from space (Stephens *et al.* 2002).

Fallspeeds of ice crystals remain a significant uncertainty, and contribute to the spread in results from different models for clouds containing ice (Starr *et al.* 2000). The radiative balance of global models has also been shown to be very sensitive to the specification of fallspeeds (Heymsfield and Iaquinta 2000). Time-averaging of Doppler radar data is one method that has been used to retrieve fallspeeds (Matrosov *et al.* 1994; Matrosov and Heymsfield 2000), and in this paper this technique is applied to both real and simulated data and is used to evaluate the fallspeeds in the model.

Section 2 briefly describes the quantities retrieved from the 94 GHz radar and the 905 nm lidar at Chilbolton, UK. Section 3 describes the altocumulus case studied in this paper. Section 4 describes the LEM, including the model initialization and the simulation of the observational data within model. Section 5 compares the real and simulated data as well as exploring the relationships between the quantities observed by the radar and the model variables. This allows us to test not only the liquid-water content (LWC) and IWC, but also the vertical winds and fallspeeds simulated by the LEM. The importance of the LWC to the radiative processes in the cloud is examined in section 5(e).

* A satellite designed to study the effects of clouds on climate and weather.

† Cloud-Aerosol Lidar and Infrared Pathfinder Satellite Observation.

2. DATA FROM THE CHILBOLTON 94 GHz DOPPLER RADAR AND 905 NM LIDAR

(a) *The Chilbolton 94 GHz Doppler radar*

The 94 GHz radar at Chilbolton has been in near continuous operation since 1996 and Doppler data has been available since 2001. The radar emits 6250 pulses per second, each equivalent to around 60 m in length and, at 7 km, about 70 m wide. The pulses are averaged in real-time to obtain 1.25 s resolution. Every thirty seconds the following parameters are calculated from these 1.25 s data:

1. the mean radar reflectivity factor, Z —this (in combination with temperatures from a forecast model) is then used to estimate the mean IWC (Hogan *et al.* 2006);
2. the mean Doppler velocity, V_D , using only the data where a detectable signal was returned;
3. the standard deviation in the Doppler velocities, $\sigma(V_D)$, only if a detectable signal was present for all 24 1.25 s intervals—this parameter provides information on turbulence (Bouniol *et al.* 2003);
4. the mean spectral width of the Doppler velocities, using only the data where a detectable signal was returned—this parameter can be difficult to interpret because it contains information from both turbulence and the spread of terminal fallspeeds, and so it is not used in this paper (although simulating this parameter may allow a better understanding of its significance, as discussed in section 5(c)).

In ice clouds the measured Doppler velocity is a function of the vertical velocities of the ice particles in the radar beam, and so depends on both the terminal fallspeeds of the ice and the vertical velocity of the air. The radar backscatter is more sensitive to the larger particles (in the Rayleigh scattering regime it is sensitive to the radius to the power six, or the mass squared), so the Doppler velocity retrieved, V_D , is the sum of the vertical air velocity, w , and the mass-squared-weighted fallspeed, V_Z :

$$V_D = w - V_Z = w - \frac{\int_0^\infty n(M)V(M)M^2 dM}{\int_0^\infty n(M)M^2 dM}. \quad (1)$$

$V(M)$ is the terminal fallspeed of an ice particle of mass M and $n(M) dM$ is the number concentration of ice particles with mass between M and $M + dM$. At 94 GHz, Rayleigh scattering is a reasonable approximation if there are not a significant number of particles with diameters larger than $\simeq 1$ mm, which is supported by the radar data and the LEM in this case. The radar return can still be used to retrieve the IWC when liquid water is present because the radar return is dominated by the ice particles, which are much larger than the liquid-water droplets.

(b) *The Chilbolton 905 nm lidar*

The attenuated backscatter coefficient, β' is recorded by the Vaisala 905 nm lidar ceilometer at Chilbolton, averaged over 30 s intervals, with a 30 m vertical resolution. In the absence of multiple scattering β' is given by,

$$\beta' = \beta \exp(-2\tau), \quad (2)$$

where β is the unattenuated backscatter coefficient and τ is the optical depth between the instrument and the height of observation, z .

$$\tau = \int_0^z \alpha dz, \quad (3)$$

where α is the extinction coefficient. Lidar is sensitive to small particles, particularly liquid-water droplets, and is therefore complementary to the radar, which is dominated by larger ice particles (Hogan *et al.* 2003a). However, a thin layer of liquid water (or a deep layer of ice) can attenuate the lidar beam, resulting in an unmeasurably small backscatter from any cloud above that level.

3. THE CASE-STUDY

A case of gradually deepening cloud, which was observed ahead of a cold front on 5 September 2003, was chosen because the number of radiosonde profiles available made it relatively straightforward to initialize the LEM (section 4(a)). Figure 1(a) shows deepening inhomogeneous ice cloud over the radar from 0500 to 1200 UTC. A comparison of the lidar (Fig. 2) and radar data shows that the ice was falling from a layer of liquid water at the cloud top ($\simeq -20^\circ\text{C}$ at 6 km); the first published explanation of such layers, where updraughts allow the condensate supply rate to exceed the ice-crystal growth rate, was given by Rauber and Tokay (1991). We expect that the large values of $\sigma(V_D)$ near cloud top (Fig. 1(b) and also Figs. 4(b) and (d)) were caused by radiative cooling to space (section 5(e) shows that radiative cooling of the liquid water contributes significantly to this process). The larger vertical velocities near the cloud top, where the largest values of $\sigma(V_D)$ are observed, allow air parcels to become saturated with respect to water as well as ice, so allowing liquid water to form (as discussed by Rauber and Tokay 1991). The lidar (Fig. 2) shows that liquid water was also intermittently present near cloud base ($\simeq -13^\circ\text{C}$ at 5 km). This liquid water may form in updraughts in turbulence caused by the evaporation of falling ice. The lidar sensitivity is reduced by the sky background during the day, which explains its failure to detect the ice. The mean Doppler velocities decrease in magnitude with height (Fig. 1(c)) because larger ice particles are present lower down in the cloud.

Four radiosondes (Fig. 3) were launched from Larkhill (20 km from Chilbolton) at 0500, 0800, 1000 and 1200 UTC. These show the gradually deepening moist cloudy layer and a thin layer near cloud top ($\simeq 450$ hPa) that is saturated with respect to liquid water. The cloud was also observed by a ground-based dual-wavelength microwave radiometer at Chilbolton. This allowed the liquid-water path (LWP) to be retrieved (e.g. Westwater 1978).

Data from four numerical weather-prediction (NWP) models were obtained from the European Union's CloudNet project. Interestingly, none of these models predicted this altocumulus case accurately. The European Centre for Medium-Range Weather Forecasts (ECMWF) model (12 to 35 hour forecasts) produced cloud in the right place, but the cloud was an ice/liquid mixture with too much liquid. The fraction of ice in the ice/liquid mixture is diagnosed from temperature in the ECMWF model (Matveev 1984), and so this scheme cannot be expected to represent the position of the thin liquid-water layers. The Met Office mesoscale model (6 to 11 hour forecast) uses separate prognostic ice and water (Wilson and Ballard 1999), but produced far less cloud than observed and no liquid. Météo France (12 to 35 hour forecasts) predicted no cloud at all (the humidity was far too low). The Swedish Meteorological and Hydrological Institute (SMHI) Rossby Centre Regional Atmosphere (RCA) model (which is not SMHI's operational model) also gave a poor representation with an incorrect humidity. These errors do not all just arise from the simple representations of mixed-phase clouds used in these models, but also from synoptic or mesoscale errors in forecasts of parameters such as humidity. However, since the resolutions of these models are improving and the microphysical schemes are gradually becoming more sophisticated, it is important to

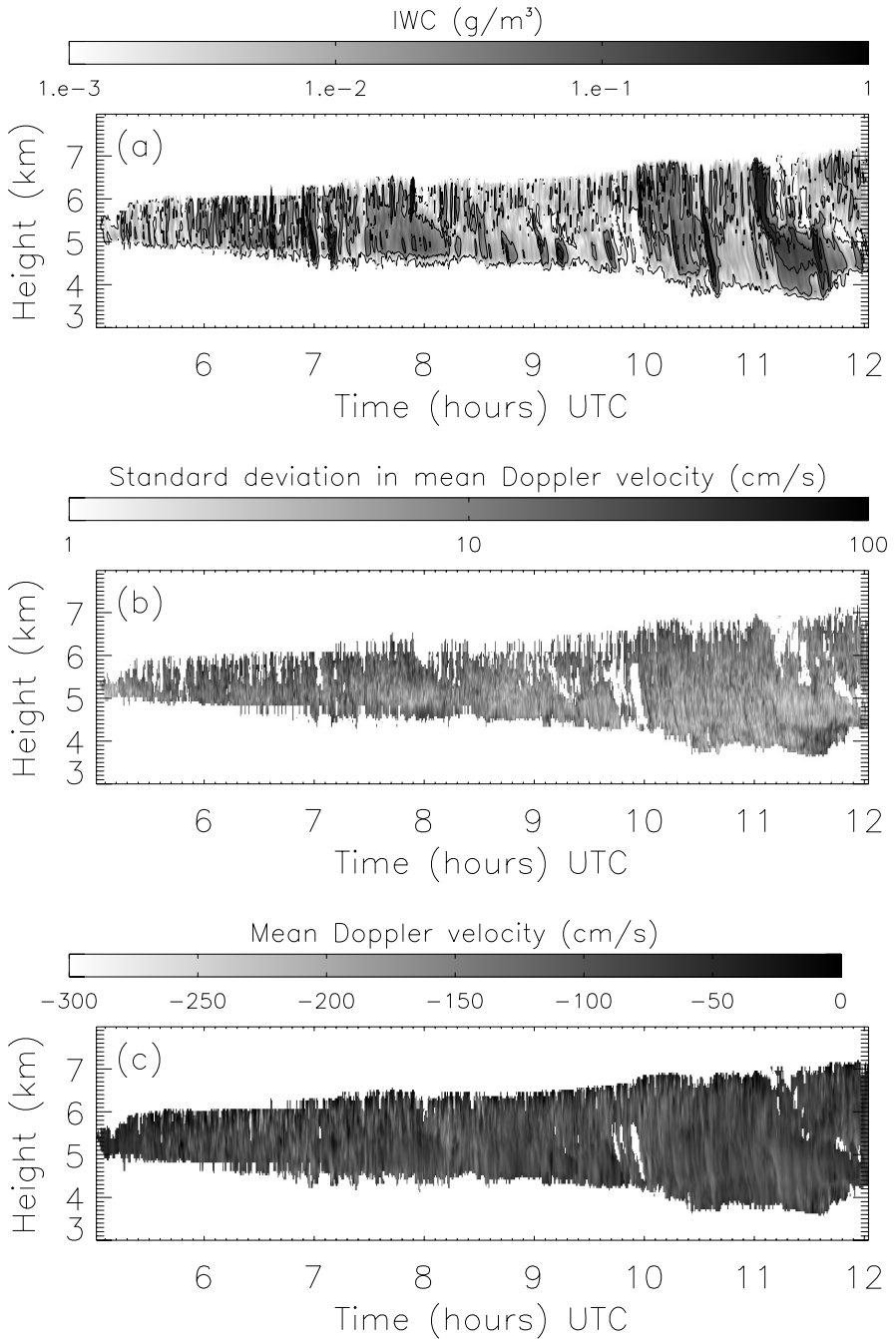


Figure 1. Observations from the Chilbolton 94 GHz radar on 5 September 2003. (a) The ice-water content from the method of Hogan *et al.* (2006) (contours at 0.001, 0.01 0.05 and 0.1 g m^{-3}), (b) the standard deviation in mean Doppler velocities, $\sigma(V_D)$, and (c) the mean Doppler velocities, V_D .

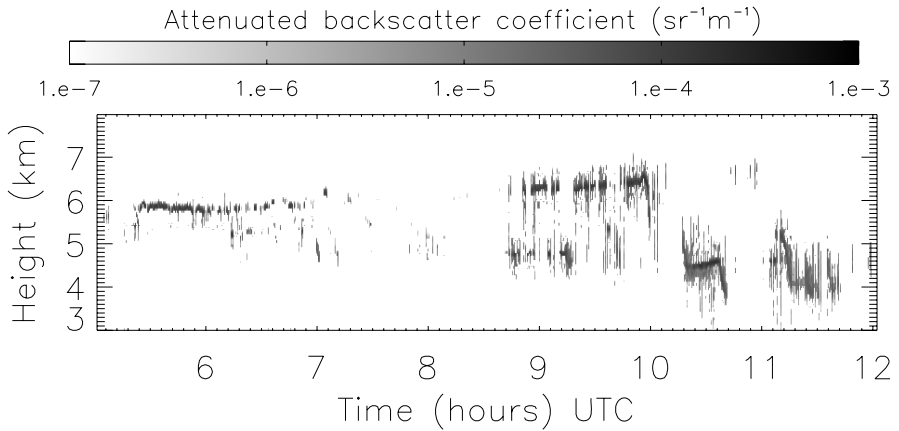


Figure 2. Observations from the Chilbolton 905 nm lidar; liquid water at the cloud top and near the cloud base gives a strong backscatter. Daylight leads to reduced sensitivity, and so the ice cannot be seen.

investigate to what extent a cloud-resolving model, such as the Met Office LEM, can capture the cloud processes involved in this case. If the LEM represents these processes well it provides a useful tool for developing parametrizations for larger-scale models.

4. METHOD

The case was simulated using an established cloud model, the Met Office LEM. In order to evaluate the modelled cloud Doppler radar and lidar data were simulated (section 4(b)). The model solves an anelastic quasi-Boussinesq set (Gray *et al.* 2001) and has a fully integrated radiation model (Fu and Liou 1992, 1993), although the effective radius of water and ice were fixed to $4.18 \mu\text{m}$ and $35 \mu\text{m}$, respectively, in the radiative code rather than being derived from the LEM fields. The radiation model is four-stream with six solar and twelve infrared bands and uses the independent-column approximation. Ice is treated optically assuming hexagonal shapes (Fu 1996; Fu *et al.* 1998) and a time-varying solar zenith angle was used. Double moment ice and snow* (i.e. prognostic mass and number) were used as well as prognostic water vapour and liquid water. The model was run in two dimensions, which is not unusual for CRM studies (e.g. Starr *et al.* 2000; Xu *et al.* 2002). It would be straightforward to apply the method of simulating the Doppler radar data to a three-dimensional study, but unfortunately the computational cost prevented this. Periodic lateral boundary conditions were used, with a rigid lid and no fluxes at the surface. Rayleigh damping was applied above 10 km to remove gravity waves. Spatial resolutions of 100 m in the horizontal and 125 m in the vertical were used, which necessitated an LEM time step of ≈ 0.8 s.

(a) *Initializing the LEM*

The four radiosonde profiles, from 0500, 0800 1000 and 1200 UTC (Fig. 3) were used to initialize the model. Radiosondes sample the near-instantaneous state of the atmosphere at particular points, whilst we wanted to initialize the LEM with mean values. The four wind-speed profiles were very similar, but using any individual profile

* Aggregated ice is called ‘snow’ in the LEM.

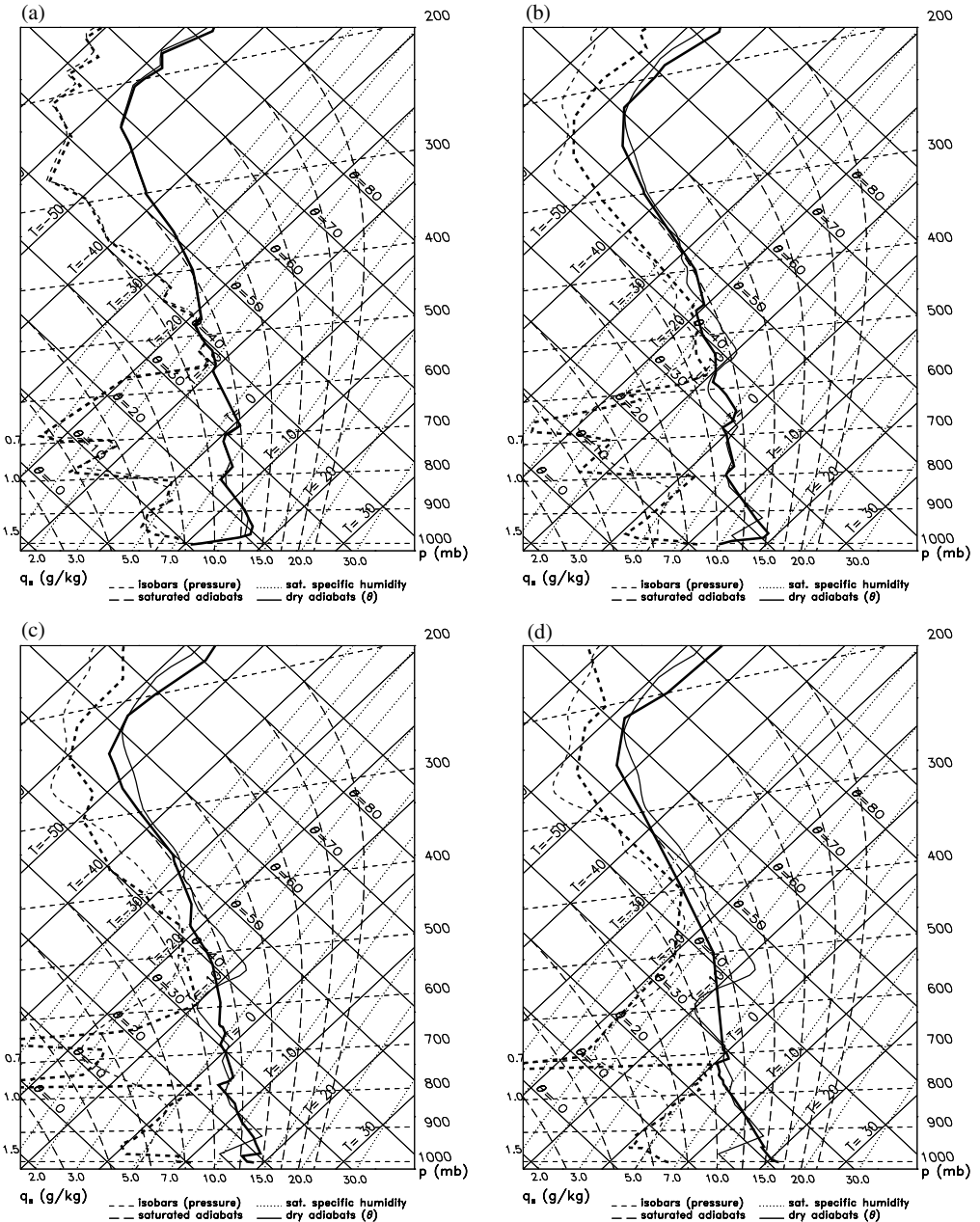


Figure 3. Observed radiosonde profiles (thick lines) from Larkhill on 5 September 2003 at (a) 0500, (b) 0800, (c) 1000 and (d) 1200 UTC. Note the thin layer at cloud-top that is saturated with respect to liquid water. Modelled profiles from the unforced model run are shown by the thin lines (these model results are discussed in section 5(a)).

generated an artificially large shear, so the model was initialized with the mean wind-speed profile. The shear below 5.5 km produces the slanting fallstreaks observed in Fig. 1.

The potential-temperature and water-vapour profiles in the model were initialized with the 0500 UTC radiosonde profile. Two model runs were then compared. In the first, the model was allowed to evolve freely. In the second, in order to account for

large-scale ascents and descents, the horizontally averaged potential-temperature and humidity data in the LEM were relaxed to a value interpolated from the time-series of radiosonde data (using a relaxation timescale of one hour). Using either method, random perturbations of ± 0.1 K and $\pm 5\%$ were added to the initial potential-temperature and water-vapour mixing-ratio fields between 4 and 8 km to allow cloud inhomogeneities to develop (Starr *et al.* 2000). In both cases the modelled turbulent kinetic energy increased rapidly for two hours and then more slowly. For this reason the first two hours of the simulations were considered to be model spin-up periods. Further simulations, using surface fluxes from the Met Office Unified Model, showed that neglecting surface fluxes had a negligible impact on the cloud for this case. Differences between results from the forced and unforced simulations are discussed in section 5(a).

(b) *Simulating the Doppler radar and backscatter lidar data within the LEM*

An LEM profile was extracted every time step, and statistics were calculated every 30 s in order to simulate the radar data (as was done for IWC by Marsham and Dobbie 2005). Statistics were calculated for the central column of the LEM. These statistics were calculated in the same way as the radar statistics, except that: (1) since at some times the LEM time step was less than 1.25 s there were between 36 to 40 time steps in any 30 s interval, rather than the 24 intervals used in the radar data; and (2) the LEM grid spacing was 100 m in the horizontal and 125 m in the vertical in the cloudy region, whereas the radar beam is 70 m in the horizontal and 60 m in the vertical at 7 km. The mean IWC* was calculated using all time steps within the 30 s interval.

The mean Doppler velocity was calculated using all time steps where there was detectable ice (i.e. greater than 2.0×10^{-4} g m⁻³, the detection limit of the radar) and the standard deviation in Doppler velocity was calculated if at least 24 time steps had detectable ice. Overall, it is thought that errors introduced by this difference in the basic time-averaging interval of the data (1.25 s for the radar, $\simeq 0.8$ s for the LEM) and the difference between the spatial resolution of the radar and the LEM are small in this intercomparison.

To output the Doppler radar statistics from the LEM the fallspeeds routinely calculated for ice and snow in the model had to be converted to a mean mass-squared-weighted fallspeed to replicate the Doppler radar data (see the appendix). In addition to the IWC and Doppler velocities observable by the radar, LEM modelling also allowed statistics of unobservable parameters, such as vertical winds and fallspeeds, to be generated with the same averaging in time and space. This then allows us to investigate the relationships between the observable and unobservable parameters for this modelled altocumulus cloud (section 5(c)), thus the LEM simulation can be used as a test for retrieval algorithms that estimate these ‘unobservable’ parameters from observable ones.

In order to simulate the lidar data, the extinction coefficient, α_i , of a hydrometeor species, i , was assumed to be

$$\alpha_i = 1.5 \times \text{WC}_i / (\rho_i r_{ei}), \quad (4)$$

where WC_i is the water content of species i (i.e. the LWC or the IWC), ρ_i is the density of liquid water or ice and r_{ei} is the effective radius (Foot 1988). Effective radius is not a prognostic variable for liquid water in the LEM so a value of $4.18 \mu\text{m}$ was used (as used for the radiative transfer; the minimum value allowed by the parametrization used). This radius was consistent with radii derived from the LWC using the number concentration

* The IWC was output from the LEM, not a radar reflectivity from which IWC could be derived; in this sense the IWC data are not true ‘simulated data’.

of $2.4 \times 10^8 \text{ m}^{-3}$ assumed by the LEM and also *in situ* observations from other similar mixed-phase clouds (Hogan *et al.* 2003a). The effective radius for ice and snow were derived from the mass and number concentrations in the LEM. β was estimated using α divided by a ‘lidar ratio’, or ‘extinction-to-backscatter ratio’, S ,

$$\beta_i = \alpha_i / S_i. \quad (5)$$

A value of S of 18.5 sr was assumed for both ice and liquid water. This is an appropriate value for liquid water (Pinnick *et al.* 1983) and a reasonable mean value for ice, although the value for ice is much more variable, typically 15–50 sr (Grund and Eloranta 1990), although 5–150 sr has been observed for cirrus (Lynch *et al.* 2002). The backscatter values were then summed for each hydrometeor species and applied in Eqs. (2) and (3) to get the attenuated backscatter coefficient, β' , at each level.

5. RESULTS

We first compare results from the unforced and forced simulations with observed values (section 5(a)). This shows that profiles from the unforced simulation differ significantly from those observed and, in this case, the modelled cloud is higher than observed. The unforced model run does not account for large-scale ascents or descents and ECMWF 12 to 24 hour forecasts suggest that allowing for these would produce model profiles more similar to those observed. Relaxing the profiles to those observed (to account for these unresolved large-scale processes) results in a cloud more similar to the one observed, and results from this run are used in the remainder of the paper (sections 5(b) to (e)).

(a) *The unforced and forced simulations*

Figure 3 shows the observed radiosonde profiles compared with profiles from the freely evolving model run. This shows that by 0800 UTC the modelled temperature within the cloud-layer was higher than observed (580 to 450 hPa, \simeq 4500 to 6300 m), due to the latent heat released by condensation and freezing. Similarly, below the cloud the modelled temperature was lower than observed (680 to 580 hPa, \simeq 3200 to 4500 m), due to sublimation of ice. These deviations from the observed profile grew throughout the simulation until 1200 UTC, at an overall rate of approximately 1 K hour^{-1} . Vertical winds from the 12 to 24 hour ECMWF forecasts suggest a large-scale ascent rate of up to 3 cm s^{-1} at 8 km and a descent of up to 2 cm s^{-1} at 4.5 km. If these ascents were adiabatic they would largely compensate for the observed deviations of the modelled profiles from those observed. Figure 4(a) shows that the unforced model run results in IWCs comparable with those observed, but the cloud is higher than observed. Figure 4(b) suggests that turbulence levels were similar to those observed, but larger at cloud top. This may have led to the cloud-top height increasing too rapidly with time and to the cooler than observed cloud top at 0800 UTC (Fig. 3).

Continuously relaxing the model profile to the observed profiles (section 4(a)) gave a better agreement with the observed temperature profiles, as expected (dew-point and air temperatures within approximately 2 K of those observed). The ECMWF forecasts suggest significant large-scale ascents and descents of $2\text{--}3 \text{ cm s}^{-1}$ but, without a more complete set of observations that would allow these large-scale effects to be more accurately quantified (e.g. Zhang and Lin 2001), it is not possible to evaluate to what extent the relaxation is accounting for the unresolved large-scale processes, or to what extent it is an artificial forcing. However, since we cannot expect the LEM to represent

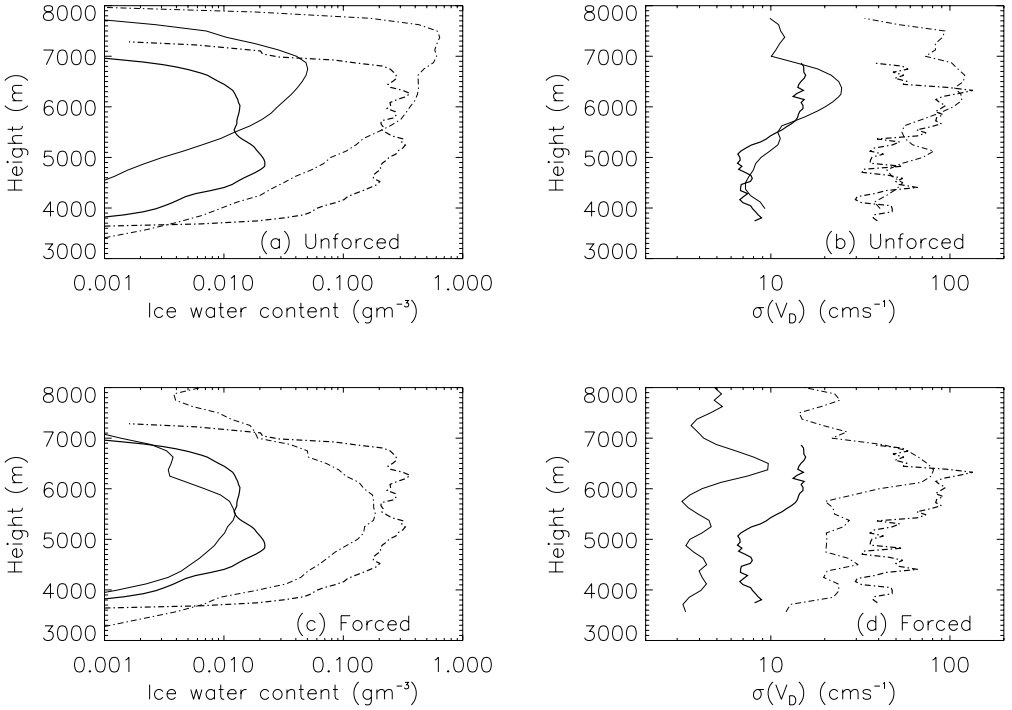


Figure 4. Profiles (a) and (c) of ice-water content, and (b) and (d) of the standard deviation in mean Doppler velocity, $\sigma(V_D)$, both between 0700 and 1200 UTC. Thick and thin lines show observed and modelled values, respectively. Mean values are shown by the solid lines and the maximum values by the dash-dot lines. Statistics of $\sigma(V_D)$ were only calculated where this parameter was defined (i.e. when a detectable signal was present for all the contributing time intervals). Panels (a) and (b) are from the unforced simulation, and (c) and (d) from the run relaxed to the time-series of observed profiles.

the cloud accurately without accounting for these large-scale processes, the results from the forced model run are used throughout the remainder of the paper.

The run relaxed to the observed profiles captures the observed IWC profile (mean and maximum values) reasonably well, but the observed values at some levels are up to five times the modelled values (Fig. 4(b)). This is outside the error bounds of the observations, which are less than a factor of two (Hogan *et al.* 2006). Overall, the modelled IWP is 0.6 times that observed. The relaxation of the model profile towards those observed has reduced the cloud-top height compared with the unforced run and allowed the cloud to deepen more by moistening air below 580 hPa. The relaxation reduces the turbulence in the cloud, however, leading to less turbulence than observed (Fig. 4(d)).

(b) Comparing observed and modelled fields

Figure 5 shows the simulated time–height cross-sections of IWC, the standard deviation in Doppler velocity and mean Doppler velocity. More quantitative comparisons of IWC and Doppler velocities are shown in subsequent figures, which show probability density functions (pdfs) of the variables, their interdependence and their height dependence. Again considering 0500 to 0700 UTC as a spin-up period (section 5(a)), comparing Figs. 1(a) and 5(a) shows that the LEM captures the spatial variability of the IWC remarkably well, although there is more ice above 8 km in the model and too much

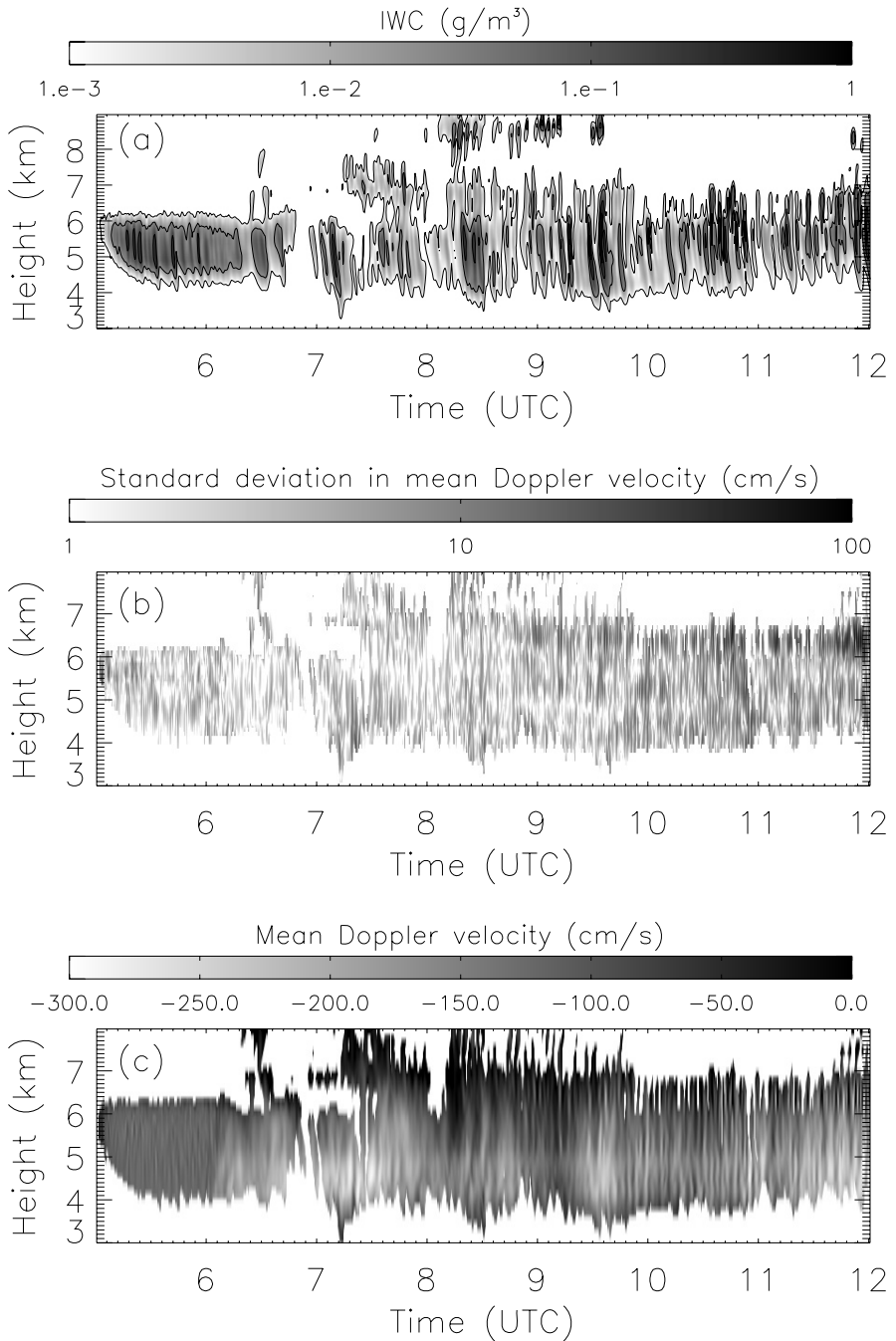


Figure 5. Simulated radar retrievals from the LEM showing (a) the ice-water content (contours are at 0.001, 0.01, 0.05 and 0.1 g m^{-3}), (b) the standard deviation in mean Doppler velocity, and (c) the mean Doppler velocity. The corresponding observations are shown in Fig. 1.

ice at 7 km before 1000 UTC. The orientation and scales of the features are similar in the real and simulated observations. Similarly, comparing Figs. 1(b) and 5(b) we see that the model is capturing the increase in the standard deviation in mean Doppler velocity with height (and hence the standard deviation in vertical air velocity, section 5(c)), which is caused by the long-wave cooling of the cloud top (also see Fig. 4(d)) and also some patchy increases in turbulence near the cloud base. The values are, however, in general too small. The mean Doppler velocities decrease with height in both the model and the observations (Figs. 1(c) and 5(c)), but it should be noted that the simulated mean Doppler velocities are affected by waves in the LEM. The mean vertical wind at any level in the LEM is zero, so time-averaging data from time–height plots of true air velocities was expected to produce velocities close to zero for long time intervals. This did not occur, and this was probably caused by waves propagating in the LEM that had a phase speed similar to the wind speed, but in the opposite direction (the effect was removed if the ‘radar position’ in the LEM was randomly varied at each time step). Such waves may be artificially maintained by the periodic lateral boundary conditions used in the LEM, but the effect was robust to damping vertical velocities and potential temperatures at the edge of the model domain and varying the strength of the Rayleigh damping layer. The waves were not caused by relaxing to the time-series of radiosonde data, and occurred in unforced model runs (section 4(a)), or runs using a constant wind speed rather than a sheared profile. However, these waves had a horizontal wavelength of approximately 5 km and so affected the cloud on a timescale of approximately 5 min (wind speed $\simeq 15 \text{ m s}^{-1}$) and are expected to have relatively little effect on the cloud.

The attenuated lidar backscatter from the ice is apparently much larger in the LEM (Fig. 6(a)) than in the observations (Fig. 2). It is not clear though whether in reality we should be able to observe this modelled backscatter from the ice, since the lowest recorded attenuated backscatters in the observations are a function of the instrument (caused by the proximity of layers giving significant backscatter) rather than real observations. The daylight also reduces the sensitivity of the instrument. The extinction-to-backscatter ratio, S_{ice} , may also have been underestimated (a value of 30 sr would halve β'). The LEM produces liquid-water cells near cloud top ($\simeq 6.8 \text{ km}$) as observed (Fig. 2). It clearly captures the cellular nature of the LWC. The base of each liquid cell is detected by the real and simulated lidar, but the beam is rapidly attenuated and in the LEM the liquid-water cells are in fact 100 m to 600 m deep (Fig. 6(b)). The LEM produces less liquid cloud than observed near cloud base (this was also true for the unforced run, which had turbulence levels more similar to those observed (Fig. 4)). Figure 7(a) shows that the LEM tends to overestimate the mean attenuated backscatter at 5 to 6 km compared with the observations but, as already noted, the backscatter from the ice is larger in the LEM than in the observations. The LEM shows peaks in backscatter from the liquid layers and the magnitude of the peaks is comparable with the observed values (Fig. 7(b)).

Figure 8 compares the LWP retrieved from the microwave radiometer data and the LEM data. The radiometer beam width is 2.3° , giving an instantaneous field-of-view of 200 m by 200 m at a height of 5 km. This is smaller than the size of the liquid-water cells in the LEM ($\simeq 1 \text{ km}$). Figure 8 shows that the maximum LWP observed in a single column of the LEM is approximately half the magnitude of the microwave-radiometer retrievals, whilst the mean LWP in the LEM is 10 to 20% of that observed. This shows that the LEM is producing significantly fewer cells than occurred in reality, which each have a lower LWP than in reality. This hypothesis is supported by photographs from the Chilbolton cloud camera, which showed a continuous liquid-water layer with a cellular structure. Persistent supercooled liquid layers in a mixed-phase cloud have

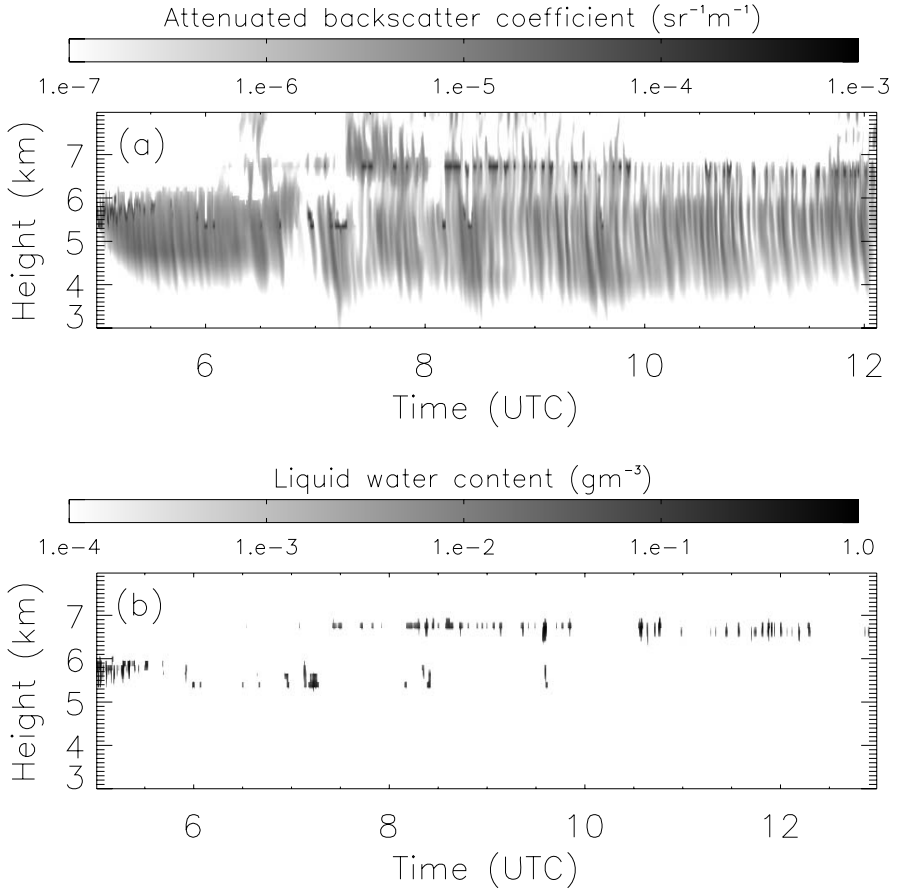


Figure 6. (a) Simulated attenuated lidar backscatter from the LEM, and (b) the corresponding modelled liquid-water content. Observed lidar data is shown in Fig. 2.

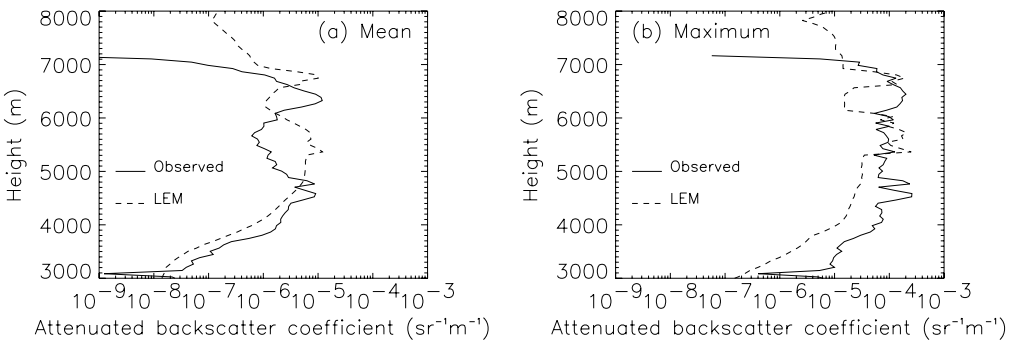


Figure 7. Attenuated lidar backscatter coefficient for the observed (solid line) and simulated (dashed line) data between 0700 and 1200 UTC. Horizontal (a) means and (b) maxima are shown as a functions of height.

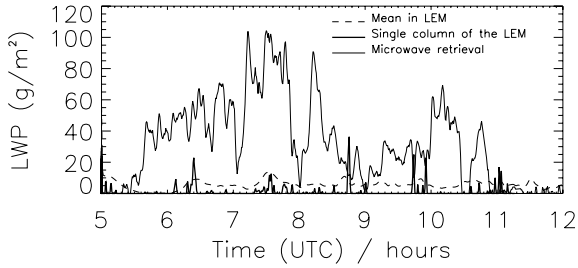


Figure 8. Liquid-water paths from the LEM compared with microwave retrievals. ‘Single column of the LEM’ refers to the central column of the model.

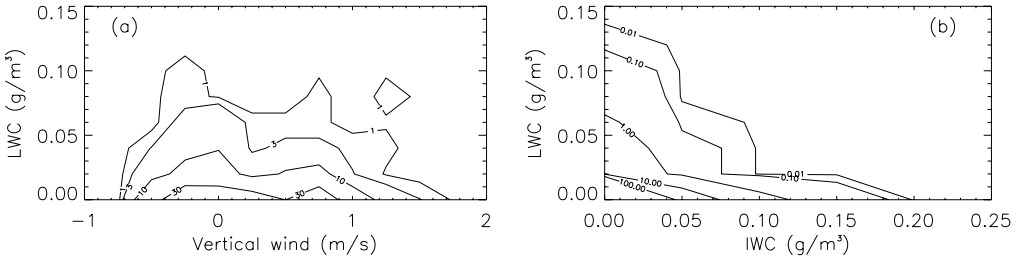


Figure 9. Bivariate probability density functions of (a) liquid-water content (LWC) and vertical winds (for LWCs greater than $2.0 \times 10^{-3} \text{ g m}^{-3}$) and (b) ice-water content (IWC) and LWC (where either the LWC or the IWC is greater than $2.0 \times 10^{-3} \text{ g m}^{-3}$) from the LEM data between 0700 and 1200 UTC.

to be convectively overturning, otherwise the liquid water depleted by glaciation will not be replenished. Therefore, the LWC profile within the liquid cells should be close to adiabatic. The LWP of the liquid cells in the LEM are slightly subadiabatic and the microwave observations show that there are too few of them. The unforced model run gave larger than observed vertical velocities at cloud top (Fig. 4(b)), but this only increased the LWP to 30% of that observed. Using prognostic ice nuclei (IN) in the LEM would allow ice nucleation, growth and fallout to deplete IN concentrations, and so may allow more liquid water to form in the model—as shown by Cotton and Brown (2004) for an idealized altostratus cloud and Rasmussen *et al.* (2002) and Geresdi *et al.* (2005) for freezing drizzle formation. Decreasing the heterogeneous nucleation rate in the LEM (Meyers *et al.* 1992) by a factor of five did increase the LWP in the model by a factor of approximately 2.3 and decreased the IWP by 15%. This LWP is in better agreement with the observations, which supports this hypothesis. However, with a decreased heterogeneous nucleation rate, mean mass-squared-weighted fallspeeds were increased by approximately 4%, presumably because fewer ice particles allowed increased particle growth rates from vapour deposition, which is in poorer agreement with the observations (section 5(d)). Finally, Fig. 9(a) shows that in the LEM most of the liquid water tends to be in the updraughts, as expected. In addition, there is significant coexistence of liquid water and ice in the model. Figure 9(b) shows that ice and liquid water coexist on the 100 m grid scale of the LEM—as observed by Field *et al.* (2004) in aircraft data—although larger values of IWC tend to be found for lower values of LWC and higher values of LWC tend to occur with lower values of IWC.

Figure 10(a) shows that the pdfs of IWC in the model and observations are similar, although the probability of any value of IWC greater than 0.03 g m^{-3} is up to three times as likely in the radar data, and values less than 0.03 g m^{-3} are more likely in

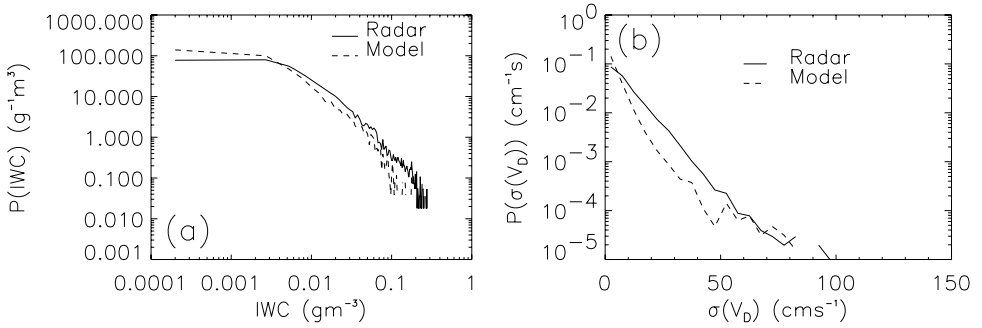


Figure 10. Probability density functions of (a) ice-water content (IWC), and (b) standard deviation in mean Doppler velocities, $\sigma(V_D)$, between 0700 and 1200 UTC. Statistics are only calculated between heights of 3000 to 8000 m and where (a) the IWC is greater than $2.0 \times 10^{-4} \text{ g m}^{-3}$, and (b) $\sigma(V_D)$ is greater than 1 cm s^{-1} .

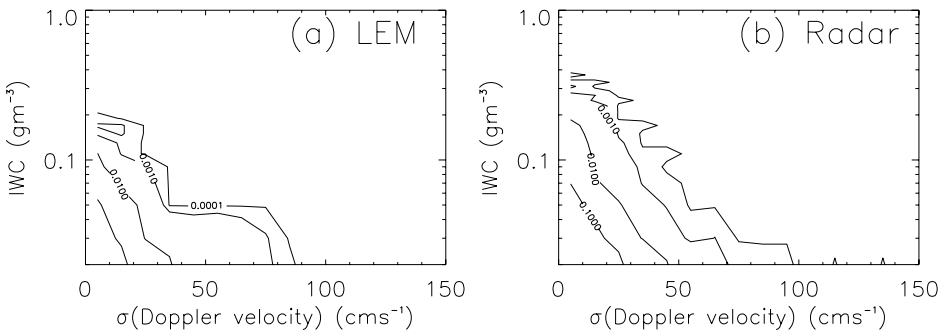


Figure 11. The bivariate probability density functions of ice-water content (IWC) and the standard deviation in mean Doppler velocities, $\sigma(V_D)$, from (a) the LEM data and (b) the radar between 0700 and 1200 UTC. Statistics have been calculated for data between heights of 3000 and 8000 m and where the IWC is greater than $2.0 \times 10^{-4} \text{ g m}^{-3}$ and $\sigma(V_D)$ is greater than 1 cm s^{-1} .

the model. Comparing the observed and modelled pdfs of standard deviation in mean Doppler velocity (Fig. 10(b)) shows that the LEM gives far fewer values between 7 and 50 cm s^{-1} . Figure 11 shows that the relationship between IWC and $\sigma(V_D)$ is similar in the model and observations, with large standard deviations in Doppler velocities tending to occur with low IWC; these occur at the edge of the convective cells in the LEM. The relative magnitudes of the distributions differ, however, since there are differences between the modelled and observed pdfs of IWC and $\sigma(V_D)$ (as noted for Fig. 10).

(c) *The modelled relationship between standard deviations in Doppler velocities and air velocities*

An advantage of simulated radar data is that the modelled standard deviation in Doppler velocity, $\sigma(V_D)$, can easily be compared with the modelled standard deviation in air velocity, $\sigma(w)$. This allows the hypothesis that $\sigma(w)$ dominates $\sigma(V_D)$ in ice clouds (Bouniol *et al.* 2003) to be tested. Figure 12(a) shows that this is true in this mixed-phase cloud, particularly for standard deviations greater than 12 cm s^{-1} . For values of $\sigma(V_D)$ less than 12 cm s^{-1} , $\sigma(V_D)$ tends to provide an overestimate of $\sigma(w)$. This occurs because the variance in V_Z becomes comparable with the variance in w for small values of w (Fig. 12(b)). This contribution of $\sigma(V_Z)$ to $\sigma(V_D)$ is larger than that observed by Lothon *et al.* (2005) for marine stratocumulus, since the fallspeeds of

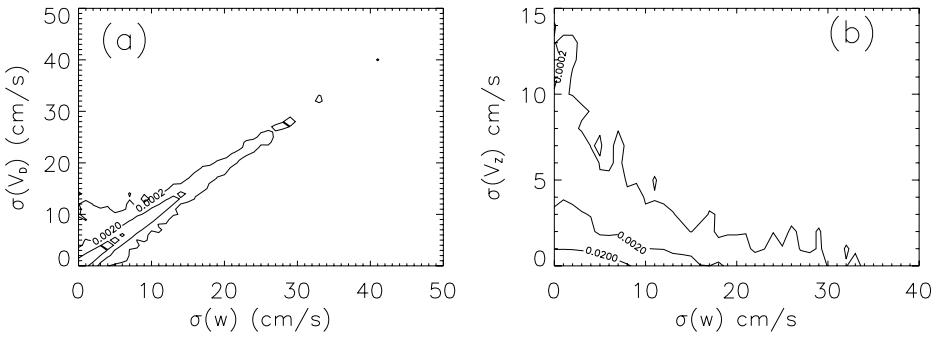


Figure 12. Bivariate probability density functions of (a) simulated standard deviations in Doppler velocities, $\sigma(V_b)$, and vertical air velocities, $\sigma(w)$, and (b) simulated standard deviations in vertical air velocities, $\sigma(w)$, and mass-squared-weighted fallspeeds, $\sigma(V_z)$. Data from between 0700 and 1200 UTC were used and contours are at 2×10^{-4} , 2×10^{-3} and 2×10^{-2} in both plots.

ice and snow are more comparable with the vertical air velocities than the fallspeeds of liquid cloud droplets.

We expect the standard deviation in Doppler velocities to depend not only on the magnitudes of the vertical air velocities, but also on the structure of the embedded convection. So, even though standard deviations in Doppler velocities are dominated by the standard deviations in air velocities, it is difficult to compare modelled spatial fields of vertical velocities and observed time–height cross-sections of standard deviations in Doppler velocities, without simulating the spatial and temporal sampling of the radar within the LEM (as we have done).

The success of this approach in evaluating the relationship between $\sigma(w)$ and $\sigma(V_z)$ suggests that it may be worth following a similar approach to investigate observed Doppler spectral widths. The subgrid vertical velocities and subgrid variance of fallspeeds in the LEM (from the assumed gamma distribution of particle sizes) could be combined to give a simulated Doppler spectral width. This may allow the relative contributions of the variations in vertical velocities and fallspeeds to Doppler spectral width to be evaluated.

(d) *Time-smoothing Doppler velocities to retrieve fallspeeds*

Time-averaged observed Doppler velocities and time-averaged mass-squared-weighted fallspeeds from the LEM were compared to evaluate the fallspeeds in the LEM. Time-averaging Doppler radar velocities is intended to remove the time-varying contribution of the vertical winds, allowing retrieval of mass-squared-weighted fallspeeds (e.g. Matrosov *et al.* 1994; Matrosov and Heymsfield 2000). However, the simulated radar data did not allow the accuracy of the time-averaging method to be evaluated for this cloud since, as noted in section 5(b), time-smoothing the modelled vertical winds showed that these did not average to zero because of waves in the LEM. Time-averaging the radar observations also relies on the radar pointing absolutely vertically upwards. The accuracy of this is better than $\pm 0.5^\circ$ for the Chilbolton 94 GHz radar, but even an error of 0.2° will result in an error of 5 cm s^{-1} for a wind speed of 15 m s^{-1} (so this technique is best suited to less windy conditions).

Figure 13 shows that fallspeeds are larger in the LEM than in the observations. The difference is approximately 40 cm s^{-1} below 8 km. This is larger than the errors expected from any deviation of the radar from the vertical ($\approx 5 \text{ cm s}^{-1}$) or any large-scale uplift ($\approx 3 \text{ cm s}^{-1}$). It is not clear why the LEM is giving larger fallspeeds

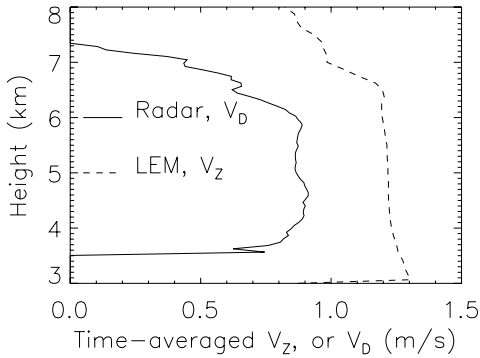


Figure 13. Time-averaged mass-squared-weighted terminal fallspeeds, V_z , from the LEM (dashed line) compared with time-averaged Doppler velocities, V_D , from the radar (solid line), using data between 0700 to 1200 UTC.

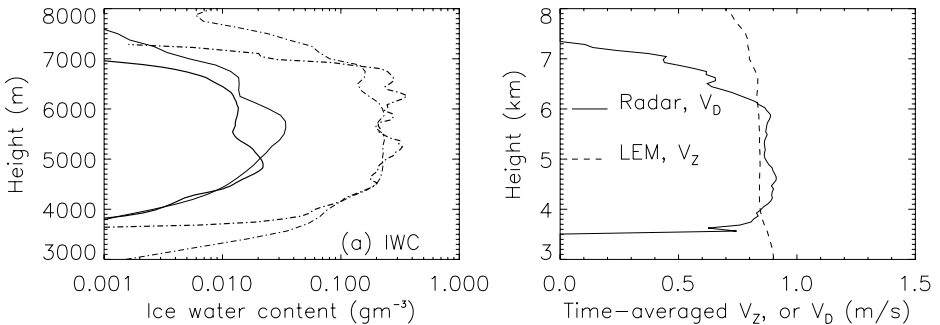


Figure 14. Data from a run with reduced fallspeeds (two thirds their standard values): (a) as Fig. 4(a), and (b) as Fig. 13.

than observed, especially since the modelled IWC is lower than observed (Fig. 4(c)). Without observations of particle size we do not know if the LEM is overestimating the particle sizes, or whether it is overestimating the terminal fallspeeds of ice particles of the correct size (or both). Reducing the fallspeeds in the LEM by a factor of two thirds and rerunning the model gave a fallspeed profile in better agreement with the observations (Fig. 14(b)). This did not significantly change the mean LWP compared with the standard run (the mean LWP was increased by 4%) and gave larger IWC, up to twice those observed (Fig. 14(a)).

Figure 15 shows the time-smoothed data from half-hour intervals, for which there was data for all the 30 s intervals used in the time-smoothing. The modelled distribution is too bimodal, due to the distinct classes of ice and snow in the LEM. The fallspeeds are not well correlated with the IWC in either the observations or the model, and there is a wide spread of fallspeeds for any IWC. This result suggests that, although a parametrization of fallspeeds based on IWC (for example Matrosov and Heymsfield 2000, for ice clouds) may be better than using a fixed value, it is by no means ideal (since large numbers of small crystals can give large IWCs with low fallspeeds and a small number of large crystals can give the same IWC, with much larger fallspeeds).

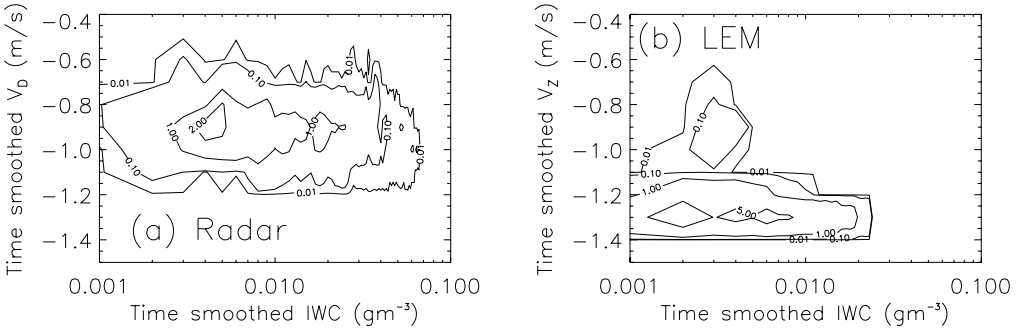


Figure 15. Bivariate probability density functions of time-averaged ice-water content and (a) Doppler velocities from the radar, and (b) fallspeeds from the LEM. Time-averaging was performed over 30 min intervals for heights between 3 km and 8 km.

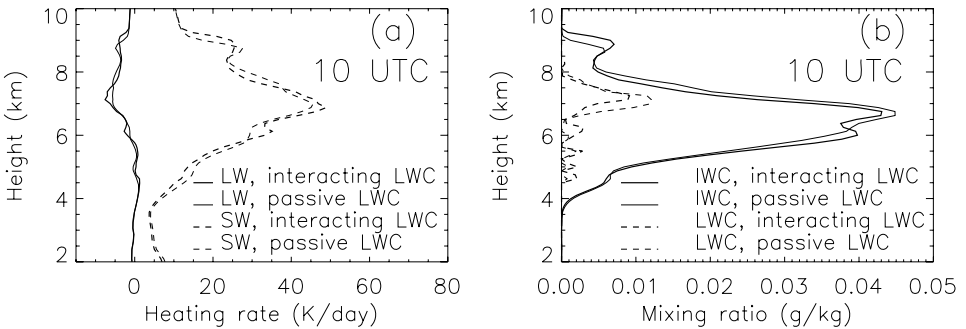


Figure 16. Modelled profiles of (a) radiative heating rates, and (b) mixing ratios, both at 1000 UTC. ‘Passive LWC’ indicates profiles where the interaction between the liquid-water content and the long-wave and short-wave radiation has been switched off in the model. ‘Interacting LWC’ indicates where both the ice-water content and the liquid-water content have been allowed to interact with the radiation.

(e) Contribution of liquid water to the modelled radiative processes

We expect the liquid water at cloud top to enhance long-wave cooling and reflect a significant fraction of the incoming solar radiation to space (since the small liquid-water droplets reflect the short-wave radiation more effectively than the larger ice crystals). Figure 16 shows the effects of removing the interaction between the LWC and the radiation scheme in the LEM in order to investigate to what extent these processes feed back on to the cloud structure. The LWC increases the cloud-top radiative cooling rate by up to 50% (at 7.2 km, Fig. 16(a)). It also increases the total reflected solar radiation at the top of the modelled atmosphere by up to 30 W m^{-2} , or 8% (not shown). These processes have raised the height of the maximum LWC by $\simeq 200 \text{ m}$ at 1000 UTC (Fig. 16(b)), since the LWC tends to form in the strong updrafts in the LEM, which occur at cloud top and are driven, in part, by the radiative processes.

6. CONCLUSIONS

We have simulated a case of mixed-phase altocumulus observed by the Chilbolton 94 GHz cloud radar, 905 nm lidar and a dual-wavelength microwave radiometer. Simulating the Doppler radar and lidar observations within the LEM has allowed us

to account for the temporal and spatial sampling of the observing instruments and so compare modelled and observed quantities. In addition, this has allowed us to explore relationships between observed quantities and modelled quantities, (e.g. the standard deviation in mean Doppler velocity and vertical winds). The observations have allowed us to compare modelled and observed IWC, LWP, turbulence, fallspeeds and the locations of LWC, but not ice particle sizes or number concentrations. The evaluation of the LEM is limited by the model initialization and forcing used (i.e. a relaxation to a time-series of radiosondes to account for unresolved large-scale forcings), since accurate large-scale advective tendencies are not available for the Chilbolton radar site. We have, however, provided a framework for comparison between observations and models that could be applied to sites with more complete observations, such as the Atmospheric Radiation Measurement (ARM) program sites. In addition, there are very few comparisons between models and observations of mixed-phase layer clouds in the literature, and the simulations highlight cloud processes that must be represented if mixed-phase clouds are to be well modelled by GCMs.

The LEM produced a cloud that was realistic in a number of respects: (1) the profile, pdf and time–height field of IWC were similar to those observed (the modelled IWP was approximately 60% of that observed); (2) the LEM produced a layer of supercooled water at cloud top; and (3) the standard deviations in vertical winds were 1.5 to 4 times smaller than observed (although values for the unforced model run were similar to observed). A comparison with the LWP retrieved from a dual-wavelength microwave radiometer showed that the LWPs of the liquid cells at cloud top in the LEM were too small (up to 50% of those observed), and that there were for too few liquid cells. This was also the case in the unforced model run, which had greater than observed turbulence at cloud top. It is possible that using prognostic ice nuclei in the LEM would allow depletion of ice nuclei by nucleation and so allow more liquid water to form in the model. This hypothesis is supported by the fact that when the heterogeneous ice nucleation rate was decreased by a factor of five in the LEM the modelled LWP was increased by a factor of 2.3, and the IWP decreased by 15%.

Comparing time-smoothed observed mean Doppler velocities and time-smoothed simulated mass-squared-weighted fallspeeds showed that observed fallspeeds were approximately two thirds of modelled values. Reducing the fallspeeds in the LEM so that they agreed with the observations gave similar LWC profiles to the standard run, but increased the IWC, giving an IWP 1.6 times that observed. Without observations of mean particle size, or ice number concentration, it is not clear whether the fallspeeds in the LEM are larger than observed because of overestimating the fallspeeds for particles of the correct size, or of overestimating the sizes of the particles. There was little observed or modelled dependence of fallspeeds on IWC, highlighting the limitations of basing fallspeed parametrizations on only the IWC.

Simulating Doppler radar data within the LEM showed that, for standard deviations in Doppler velocities, $\sigma(V_D)$, greater than $\simeq 12 \text{ cm s}^{-1}$, the modelled standard deviation in Doppler velocities provided an almost unbiased estimate of the modelled standard deviation of vertical winds, $\sigma(w)$. For smaller values, $\sigma(V_D)$ tended to be an overestimate of $\sigma(w)$. Modelling Doppler spectral widths would allow a better understanding of the relative contributions of variations in vertical winds and fallspeeds to this observed parameter.

In the LEM the thin layer of liquid water at cloud top contributed significantly to the radiative cooling at the cloud top and to the short-wave reflectivity. This fed back onto the cloud dynamics to a limited extent, raising the height of the maximum LWC by 200 m.

Many NWP models failed to give a good forecast for this case. The results show the importance of using separate prognostic ice and liquid water in NWP models, using a vertical resolution that captures the thin layers of liquid water and accurately representing the subgrid vertical velocities that allow liquid water to form. The results also show the potential significance of the local depletion of ice nuclei within mixed-phase clouds, and so of using prognostic ice nuclei in the LEM. The success of the LEM in representing this case demonstrates its potential as a tool for the development of parametrizations for future NWP and climate models.

ACKNOWLEDGEMENTS

The authors would like to acknowledge the Cloudnet project (European Union project EUK2-2000-00611) for radar, lidar and radiometer data from the Chilbolton Facility for Atmospheric and Radio Research (part of the Rutherford Appleton Laboratory) and for the NWP model output. Nicolas Gaussiat performed the microwave radiometer retrieval. Radiosonde data were obtained from the Met Office. In addition the authors would like to thank the helpful comments of the two anonymous referees. This work was funded by the Natural Environment Research Council (grant NER/M/S/2002/00127).

APPENDIX

Calculation of mass-squared-weighted fallspeeds in the LEM

As described by Gray *et al.* (2001), the LEM assumes a relationship between diameter, D , and fallspeed, $V(D)$, for each hydrometeor species, x (i.e. ice or snow in this case),

$$V_x(D) = a_x D^{b_x} \left(\frac{\rho_0}{\rho} \right)^{0.5}, \quad (\text{A.1})$$

where a_x , b_x are constants, which depend on the hydrometeor type (Gray *et al.* 2001; Lin *et al.* 1983; Ferrier *et al.* 1994), ρ is the air density and ρ_0 the surface air density. The mass, $M_x(D)$, of a particle of diameter D is

$$M_x(D) = c_x D^{d_x}, \quad (\text{A.2})$$

where c_x and d_x are again constants for each hydrometeor species (Swann 1998; Gray *et al.* 2001). A gamma distribution is assumed for the size distribution, $n_x(D)$,

$$n_x(D) = n_{x0} D^{\alpha_x} \exp(-\lambda_x D), \quad (\text{A.3})$$

where α_x is the shape parameter (Gray *et al.* 2001; Swann 1998). The double-moment scheme in the LEM (used for ice and snow in this paper) has prognostic equations for both the total number concentration, N_x , and the total mass mixing ratio, q_x . Given these variables it can be shown that the parameters for the size distribution, n_{x0} (the intercept parameter) and λ_x (the slope parameter) are given by,

$$n_{x0} = \frac{\rho N_x \lambda_x^{(1+\alpha_x)}}{\Gamma(1+\alpha_x)}, \quad (\text{A.4})$$

and

$$\lambda_x = \left\{ \frac{N_x c_x \Gamma(1+\alpha_x+d_x)}{M_x \Gamma(1+\alpha_x)} \right\}^{1/d_x}. \quad (\text{A.5})$$

The mean mass-weighted fallspeed, V_{M_x} , is then,

$$V_{M_x} = a_x \left(\frac{\rho_0}{\rho} \right)^{0.5} \frac{\Gamma(d_x + \alpha_x + b_x + 1)}{\Gamma(1 + \alpha_i + d_x)} \lambda^{-b_x}, \quad (\text{A.6})$$

(Gray *et al.* 2001). Furthermore, it can be shown that this gives a mass-squared weighted fallspeed, V_{Z_i} , of

$$V_{Z_i} = a_i \left(\frac{\rho_0}{\rho} \right)^{0.5} \frac{\Gamma(2d_i + \alpha_i + b_i + 1)}{\Gamma(1 + \alpha_i + 2d_i)} \lambda^{-b_i}, \quad (\text{A.7})$$

for a single species, i , with a weighted average required when both ice and snow are present.

REFERENCES

- Bouniol, D., Illingworth, A. J. and Hogan, R. J. 2003 'Deriving turbulent kinetic energy dissipation rate within clouds using ground based 94 GHz radar'. In Proceedings of the 31st AMS conference on radar meteorology, Seattle
- Clark, P. D., Choullarton, T. W., Brown, P. R. A., Field, P. R., Illingworth, A. J. and Hogan, R. J. 2005 Numerical modelling of mixed-phase frontal clouds observed during the CWVC project. *Q. J. R. Meteorol. Soc.*, **131**, 1677–1694
- Cotton, R. J. and Brown, P. R. A. 2004 'Ice initiation and evolution in large-eddy simulations using prognostic ice nuclei and CCN'. P. 2 in Proceedings of the 11th conference on cloud physics, Ogden, UT, USA
- Ferrier, B. S., Tao, W. K. and Simpson, J. 1994 A double moment multiple phase four class bulk ice scheme. Part II: Simulations of convective storms in different large scale environments and comparisons with other bulk parametrizations. *J. Atmos. Sci.*, **51**, 249–280
- Field, P. R., Hogan, R. J., Brown, P. R. A., Illingworth, A. J., Choullarton, T. W., Kaye, P. H., Hirst, E. and Greenaway, R. 2004 Simultaneous radar and aircraft observations of mixed-phase cloud at the 100 m scale. *Q. J. R. Meteorol. Soc.*, **130**, 1877–1904
- Fleishauer, R. P., Larson, V. E. and Vonder Haar, T. H. 2002 Observed microphysical structure of midlevel, mixed-phase clouds. *J. Atmos. Sci.*, **59**, 1779–1804
- Foot, J. S. 1988 Some observations of the optical properties of clouds. 2. Cirrus. *Q. J. R. Meteorol. Soc.*, **114**, 145–164
- Fu, Q. 1996 An accurate parameterization of the solar radiative properties of cirrus clouds for climate models. *J. Climate*, **9**, 2058–2082
- Fu, Q. and Liou, K. N. 1992 On the correlated k -distribution method for radiative transfer in nonhomogeneous atmospheres. *J. Atmos. Sci.*, **49**, 2139–2156
- 1993 Parameterization of the radiative properties of cirrus clouds. *J. Atmos. Sci.*, **50**, 2008–2025
- Fu, Q., Yang, P. and Sun, W. B. 1998 An accurate parameterization of the infrared radiative properties of cirrus clouds for climate models. *J. Climate*, **11**, 2223–2237
- Geresdi, I., Rasmussen, R., Grabowski, W. and Bernstein, B. 2005 Sensitivity of freezing drizzle formation in stably stratified clouds to ice processes. *Meteorol. Atmos. Phys.*, **88**, 91–105
- Gray, M. E. B., Petch, J., Derbyshire, S. H., Brown, A. R., Lock, A. P., Swann, H. A. and Brown, P. R. A. 2001 'Version 2.3 of the Met. Office large eddy model: Part II Scientific documentation'. APR Turbulence and Diffusion Report 276, Met Office, FitzRoy Road, Exeter EX1 3PB, UK
- Grund, C. J. and Eloranta, E. W. 1990 The 27–28 October 1986 FIRE IFO cirrus case-study—cloud optical-properties determined by high spectral resolution lidar. *Mon. Weather Rev.*, **118**, 2344–2355

- Heymsfield, A. J. and Iaquinta, J. 2000 Cirrus crystal terminal velocities. *J. Atmos. Sci.*, **57**, 916–938
- Heymsfield, A. J., Milosevich, L. M. and Slingo, A. 1991 An observational and theoretical study of highly supercooled altocumulus. *J. Atmos. Sci.*, **48**, 923–945
- Hogan, R. J., Francis, P. N., Flentje, H., Illingworth, A. J., Quante, M. and Pelon, J. 2003a Characteristics of mixed-phase clouds: Part I: Lidar, radar and aircraft observations from CLARE'98. *Q. J. R. Meteorol. Soc.*, **129**, 2089–2116
- Hogan, R. J., Illingworth, A. J., O'Connor, E. J. and Póiares Baptista, J. P. V. 2003b Characteristics of mixed-phase clouds: Part II: A climatology from ground-based lidar. *Q. J. R. Meteorol. Soc.*, **129**, 2117–2134
- Hogan, R. J., Behera, M. D., O'Connor, E. J. and Illingworth, I. J. 2004 Estimating the global distribution of supercooled liquid water clouds using the LITE lidar. *Geophys. Res. Lett.*, **31**, L05106, doi: 10.1029/2003GL018977
- Hogan, R. J., Mittermaier, M. P. and Illingworth, A. J. 2006 The retrieval of ice water content from radar reflectivity factor and temperature and its use in the evaluation of a mesoscale model. *J. Appl. Meteorol.*, **45**, 301–317
- Korolev, A. and Isaac, G. 2003 Roundness and aspect ratio of particles in ice clouds. *J. Atmos. Sci.*, **60**, 1795–1808
- Li, Z. X. and Le Treut, H. 1992 Cloud–radiation feedbacks in a general circulation model and their dependence on cloud modelling assumptions. *Climate Dyn.*, **7**, 133–139
- Lin, Y. L., Farley, R. D. and Orville, H. 1983 Bulk parametrization of the snow field in a cloud model. *J. Climate Appl. Meteorol.*, **22**, 1065–1092
- Liu, S. and Krueger, S. K. 1995 'Numerical simulations of altocumulus with a cloud-resolving model'. In Proceedings of the 5th Atmospheric Radiation Measurement ARM science team meeting, DOE CONF-9503140, San Diego, California, USA
- 1998 Numerical simulations of altocumulus using a cloud-resolving model and a mixed layer model. *Atmos. Res.*, **47–48**, 461–474
- Lothon, M., Lenschow, D. H., Leon, D. and Vali, G. 2005 Turbulence measurements in marine stratocumulus with airborne Doppler radar. *Q. J. R. Meteorol. Soc.*, **131**, 2063–2080
- Lynch, D. K., Sassen, K., Starr, D. O'C. and Stephens, G. (Eds.) 2002 *Cirrus*. Oxford University Press, New York
- Marsham, J. and Dobbie, S. 2005 The effects of wind shear on cirrus: A large-eddy model and radar case study. *Q. J. R. Meteorol. Soc.*, **131**, 2937–2956
- Matrosov, S. Y. and Heymsfield, A. J. 2000 Use of Doppler radar to assess ice cloud particle fall velocity-size relations for remote sensing and climate studies. *J. Geophys. Res.*, **105**, 22427–22436
- Matrosov, S. Y., Orr, B. W., Kropfli, R. A. and Snider, J. B. 1994 Retrieval of vertical profiles of cirrus cloud microphysical parameters from Doppler radar and infrared radiometer measurements. *J. Appl. Meteorol.*, **33**, 617–626
- Matveev, L. T. 1984 *Cloud dynamics*. D. Reidel Publ. Co.
- Meyers, M. P., DeMott, P. J. and Cotton, W. R. 1992 New primary ice nucleation parameterizations in an explicit cloud model. *J. Appl. Meteorol.*, **31**, 708–721
- Pinnick, R. G., Jennings, S. G., Chylek, P., Ham, C. and Grandy, W. T. 1983 Backscatter and extinction in water clouds. *J. Geophys. Res.*, **88**, 6787–6796
- Rasmussen, R. M., Geresdi, I., Thompson, G., Manning, K. and Karplus, E. 2002 Freezing drizzle formation in stably stratified layer clouds: The role of radiative cooling of cloud droplets, cloud condensation nuclei, and ice initiation. *J. Atmos. Sci.*, **59**, 837–860
- Rauber, R. M. and Tokay, A. 1991 An explanation for the existence of supercooled water at the top of cold clouds. *J. Atmos. Sci.*, **48**, 1005–1023
- Starr, D. O. and Cox, S. K. 1985 Cirrus clouds. Part I: Numerical experiments on the formation and maintenance of cirrus. *J. Atmos. Sci.*, **42**, 2682–2694

- Starr, D. O., Benedetti, A., 2000 'Comparison of cirrus cloud models: A project of the GEWEX cloud systems study (GCSS) working group on cirrus cloud systems'. Pp. 1–4 in Proceedings of the 13th international conference on clouds and precipitation, Reno, USA
- Boehm, M., Brown, P. A., Gierens, K. M., Girard, E., Giraud, V., Jakob, C., Jensen, E. A., Khvorostyanov, V., Koehler, M., Lare, A., Li, R., Maruyama, K., Montero, M., Tao, W., Wang, Y. and Wilson, D.
- Stephens, G. L., Vane, D. G., 2002 The Cloudsat mission and the A-train—a new dimension of space-based observations of clouds and precipitation. *Bull. Amer. Meteorol. Soc.*, **83**, 1771–1790
- Boain, R. J., Mace, G. G., Sassen, K., Wang, Z. E., Illingworth, A. J., O'Connor, E. J., Rossow, W. B., Durden, S. L., Miller, S. D., Austin, R. T., Benedetti, A. and Mitrescu, C.
- Sun, Z. and Shine, K. P. 1995 Parameterization of ice cloud radiative properties and its application to the potential climatic importance of mixed-phase clouds. *J. Climate*, **8**, 1874–1888
- Swann, H. 1998 Sensitivity to the representation of precipitating ice in CRM simulations of deep convection. *Atmos. Res.*, **48**, 415–435
- Tremblay, A. and Glazer, A. 2000 An improved modeling scheme for freezing precipitation forecasts. *Mon. Weather Rev.*, **128**, 1289–1308
- Tremblay, A., Vaillancourt, P. A., Cober, S. G., Glazer, A. and Isaac, G. A. 2003 Improvements of a mixed-phase cloud scheme using aircraft observations. *Mon. Weather Rev.*, **131**, 672–686
- Vaillancourt, P. A., Tremblay, A., Cober, S. G. and Isaac, G. A. 2003 Comparison of aircraft observations with mixed-phase cloud simulations. *Mon. Weather Rev.*, **131**, 656–671
- Warren, S. G., Hahn, J., 1986 'Global distribution of total cloud cover and cloud type over land'. NCAR Tech. Note TN-273, National Center for Atmospheric Research, PO Box 3000, Boulder CO80307-3000, USA
- London, R. M., Chervin, R. M. and Jenne, R. 1988 'Global distribution of total cloud cover and cloud type over the ocean'. NCAR Tech. Note TN-317, National Center for Atmospheric Research, PO Box 3000, Boulder CO80307-3000, USA
- Westwater, E. R. 1978 Accuracy of water-vapour and cloud liquid determination by dual-frequency ground-based microwave radiometry. *Radio Sci.*, **13**, 677–685
- Wilson, D. R. and Ballard, S. P. 1999 A microphysically based precipitation scheme for the UK Meteorological Office unified model. *Q. J. R. Meteorol. Soc.*, **125**, 1607–1636
- Xu, K. M., Cederwall, R. T., 2002 An intercomparison of cloud-resolving models with the atmospheric radiation measurement summer 1997 intensive observation period data. *Q. J. R. Meteorol. Soc.*, **128**, 593–624
- Donner, L. J., Grabowski, W. W., Guichard, F., Johnson, D. E., Khairoutdinov, M., Krueger, S. K., Petch, J. C., Randall, D. A., Seman, C. J., Tao, W. K., Wang, D. H., Xie, S. C., Yio, J. J. and Zhang, M. H.
- Zhang, M. H. and Lin, J. L. 2001 Objective analysis of ARM IOP data: Method and sensitivity. *Mon. Weather Rev.*, **129**, 295–311